








Highly sensitive active pixel image sensor array driven by large-area bilayer MoS₂ transistor circuitry

Seongin Hong ^{1,7,8}, Nicolò Zagni ^{2,8}, Sooho Choo^{1,8}, Na Liu^{1,8}, Seungho Baek¹, Arindam Bala¹, Hocheon Yoo ³, Byung Ha Kang⁴, Hyun Jae Kim ⁴, Hyung Joong Yun⁵, Muhammad Ashraful Alam⁶  & Sunkook Kim ¹ 

Various large-area growth methods for two-dimensional transition metal dichalcogenides have been developed recently for future electronic and photonic applications. However, they have not yet been employed for synthesizing active pixel image sensors. Here, we report on an active pixel image sensor array with a bilayer MoS₂ film prepared via a two-step large-area growth method. The active pixel of image sensor is composed of 2D MoS₂ switching transistors and 2D MoS₂ phototransistors. The maximum photoresponsivity (R_{ph}) of the bilayer MoS₂ phototransistors in an 8 × 8 active pixel image sensor array is statistically measured as high as 119.16 A W⁻¹. With the aid of computational modeling, we find that the main mechanism for the high R_{ph} of the bilayer MoS₂ phototransistor is a photo-gating effect by the holes trapped at subgap states. The image-sensing characteristics of the bilayer MoS₂ active pixel image sensor array are successfully investigated using light stencil projection.

¹School of Advanced Materials Science and Engineering, Sungkyunkwan University, Suwon, Republic of Korea. ²Department of Engineering “Enzo Ferrari” (DIEF), University of Modena and Reggio Emilia, Modena, Italy. ³Department of Electronic Engineering, Gachon University, Seongnam, Republic of Korea. ⁴School of Electrical and Electronic Engineering, Yonsei University, Seoul, Republic of Korea. ⁵Research Center for Materials Analysis, Korea Basic Science Institute (KBSI), Daejeon, Republic of Korea. ⁶School of Electrical and Computer Engineering, Purdue University, West Lafayette, Indiana, USA. ⁷Department of Electrical and Computer Engineering, The University of Texas at Austin, Austin, Texas 78758, USA. ⁸These authors contributed equally: Seongin Hong, Nicolò Zagni, Sooho Choo, Na Liu. ✉email: alam@purdue.edu; intel0616@gmail.com

Two-dimensional (2D) transition metal dichalcogenides (TMDs) such as molybdenum disulfide (MoS_2), molybdenum diselenide (MoSe_2), tungsten disulfide (WS_2), and tungsten diselenide (WSe_2) have been extensively studied as next-generation semiconducting materials due to their attractive electrical and optical properties^{1–9}. However, although the TMD flakes obtained via mechanical exfoliation exhibit unique properties, their use in large-scale practical applications is difficult due to their low reproducibility and large property variations^{10–17}. By contrast, various large-area growth methods for 2D TMDs have been developed for future electronic and photonic applications^{18–25}. Choi et al.²² reported a full-color active-matrix organic light-emitting diode display based on large-area MoS_2 synthesized via metal–organic chemical vapor deposition (CVD). Zhang et al.²³ reported inverter arrays based on wafer-scale MoS_2 synthesized via atomic layer deposition (ALD). Choi et al.²⁴ reported a curved single photodetector array based on MoS_2 -graphene synthesized via CVD. Large-scale growth methods for TMDs have been reported, but they have not yet been employed to synthesize active pixel image sensors, which are integrated circuits consisting of photodetectors and active transistors that can detect the incident image light and convert it into digital image signals^{26–28}.

In this study, we report on an active pixel image sensor array with a large-area bilayer MoS_2 film, which was directly synthesized on a SiO_2/Si substrate via a two-step growth method consisting of MoS_2 sputtering (first step) and sulfurization (second step) without any transfer process. The circuitry in 8×8 active pixel image sensor array consists of switching transistors and phototransistors. The phototransistor used as a photodetector in the active pixel image sensor achieves a remarkably high photoresponsivity (R_{ph}) and signal-to-noise ratio (SNR). The main mechanism responsible for the high photoresponsivity of the bilayer MoS_2 phototransistor is the photogating (PG) effect induced by light-generated holes trapped at subgap states. This explanation is supported by spectroscopic analysis and by numerical device simulations. The simulations highlight the correlation between threshold voltage (V_{th}) shift and high R_{ph} when including subgap states near the valence band edge. Moreover, both the 64 switching transistors and the 64 phototransistors based on homogeneous semiconductor (i.e., bilayer MoS_2) in the 8×8 active pixel array are systematically investigated. It is revealed that the 64 individual pixels exhibit desired electrical and optical properties and high uniformity. Finally, we demonstrate the image-sensing characteristics of the active pixel image sensor array using light stencil projection. The proposed active pixel image sensor array can potentially be used for future image-sensing applications, such as ultra-thin image sensors, transparent image sensors, artificial-intelligence photosensors, and selective light-detecting imagers^{29–32}.

Results

Structure design of bilayer MoS_2 image sensor array. The active pixel image sensor array with a large-area bilayer MoS_2 film and its pixel configuration are schematically and photographically illustrated in Fig. 1a–c and Fig. 1d–f, respectively. The designed device is composed of an 8×8 pixel array, in which the individual pixels have an opaque top-gate switching transistor and transparent top-gate phototransistor. The opaque top-gate electrode of the switching transistor can completely block the incident light, enabling the pixel selection operation without the influence of the light. By contrast, the transparent top-gate electrode of the phototransistor can successfully transmit the incident light, enabling the generation of electron–hole pairs in the MoS_2 channel. Figure 1g shows the equivalent circuit of a pixel in the active pixel image sensor array. The phototransistor was integrated into the

pixel as a photodetector instead of a photodiode, which is typically used in active pixel image sensors, resulting in a higher photoresponsivity and SNR.

Fabrication process of bilayer MoS_2 image sensor array. The presented architecture of the active pixel image sensor array was formed using a thin film process, owing to the atomically thin bilayer MoS_2 film synthesized directly on a SiO_2/Si substrate without any transfer process. Figure 2a shows the fabrication process of the pixel unit cell. The bilayer MoS_2 film was directly synthesized on the cleaned SiO_2/Si substrate via a two-step growth method. The synthesized bilayer MoS_2 film was patterned via O_2 reactive ion etching using a photoresist mask for channel isolation. Titanium/Au (10/50 nm) as the source/drain (S/D) electrodes were deposited and patterned using an electron-beam evaporator and photolithography via a lift-off technique. Aluminium oxide (80 nm) was deposited as the gate insulator via ALD. Subsequently, transparent top-gate electrodes (i.e., indium zinc oxide, IZO) and opaque top-gate electrodes (i.e., Au) were deposited via sputtering and e-beam evaporation, and patterned via photolithography with wet-etching and lift-off techniques, respectively. The details of the device fabrication are presented in the “Methods” section.

Synthesis of bilayer MoS_2 film. The two-step growth method consisting of radiofrequency (RF) magnetron sputtering and thermal CVD is schematically illustrated in Fig. 2b, c. A MoS_2 film was deposited on a SiO_2/Si substrate via RF magnetron sputtering and then loaded into a CVD chamber for sulfurization. Hydrogen sulfide gas was used as a sulfur precursor in the sulfurization of sputtering deposited MoS_2 , which could cause a homogeneous reaction. The temperature profile and gas injection conditions as a function of time are shown in Fig. 2d. The MoS_2 film synthesized via the two-step growth method shows a uniform color, indicating thickness uniformity of the MoS_2 film on SiO_2/Si substrate with the diagonal length of ~ 9.57 cm (Fig. 3a).

Characterization of bilayer MoS_2 film. High-resolution transmission electron microscopy (TEM) analysis was performed to explore the crystalline structure of the MoS_2 film. As shown in Fig. 3b, the morphology of the MoS_2 film appears smooth and consists of several grains. The corresponding fast Fourier transform pattern shows numerous spots forming halo rings, indicating that the MoS_2 film has several random crystallite orientations³³. According to Supplementary Fig. 1, the grain size is estimated to be 5–15 nm, indicating a high density of the grain boundaries. The layer number of the MoS_2 film was determined via the cross-sectional TEM image shown in Fig. 3c. The MoS_2 film consists of two layers, with an average interlayer spacing of ~ 0.6 nm, which is consistent with the theoretical and experimental values³⁴.

The MoS_2 film was characterized using Raman spectroscopy to investigate its crystallinity and number of layers. In Fig. 3d, the Raman spectrum shows two bands at 384.8 and 405.2 cm^{-1} , which correspond to the in-plane (E_{2g}^1) and out-of-plane (A_{1g}) vibration modes, respectively³⁵. As the two modes exhibit a well-defined dependence on the number of layers, the frequency difference (Δk) between the two modes is 20.4 cm^{-1} , indicating a bilayer MoS_2 film³⁶. The Raman results are consistent with those of mechanically exfoliated MoS_2 , which indicates the high crystallinity of our MoS_2 film grown via the two-step method. The thickness of the MoS_2 film was also characterized using atomic force microscopy shown in Supplementary Fig. 2. The film thickness is estimated as ~ 1.3 nm, corresponding to a typical bilayer MoS_2 ³⁷. Photoluminescence (PL) measurement was used to investigate the optical quality of the MoS_2 film. The PL

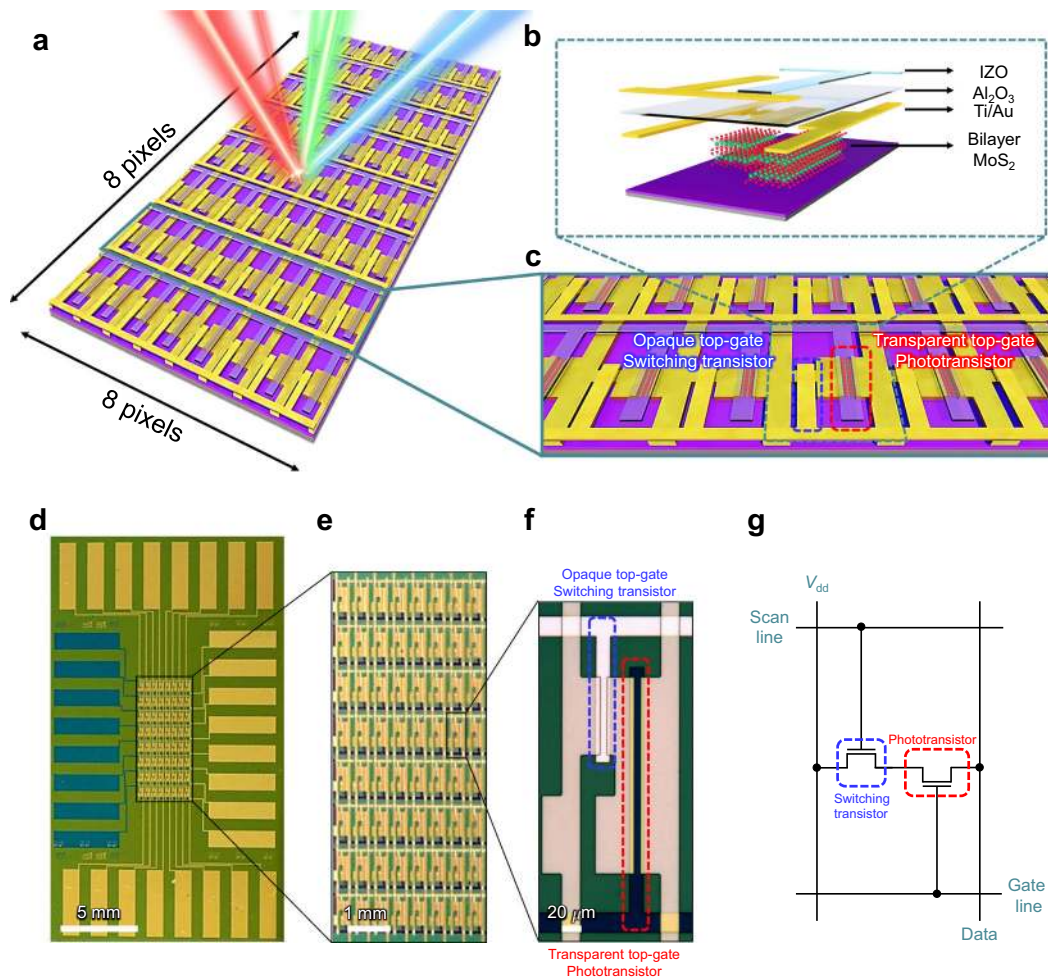


Fig. 1 Bilayer MoS₂ image sensor array. **a** Schematic illustration of an 8 × 8 image sensor array based on bilayer MoS₂. **b** Cross-section of a pixel consisting of IZO, Al₂O₃, Ti/Au, and bilayer MoS₂. **c** Image sensor array structure design composed of opaque top-gate (Ti/Au electrodes) switching transistor and transparent top-gate (IZO electrodes) phototransistor. **d** Low- and **e** high-magnification photograph of the 8 × 8 image sensor array based on bilayer MoS₂. **f** Optical microscope image of a pixel composed of opaque top-gate switching transistor (blue-dashed line) and transparent top-gate phototransistor (red-dashed line). **g** A pixel circuit diagram of proposed image sensor array. V_{dd} is drain supply voltage.

spectrum exhibits two peaks at ~663 and 617 nm, corresponding to the A1 and B1 direct excitonic transitions at 1.97 and 2.11 eV, respectively (Fig. 3e). This indicates that the PL peaks originate from the intrinsic electronic structure of the grown 2H-MoS₂³⁸. Moreover, a randomly selected area of 30 μm × 30 μm was subjected to Raman mapping. Figure 3f, g display the Raman mapping images of the intensity of the E_{2g}¹ and A_{1g} modes centered at 383 and 404 cm⁻¹, respectively. The uniform color contrast demonstrates the high crystallinity and thickness uniformity of our grown MoS₂ film at a microscale.

The chemical composition of the synthesized bilayer MoS₂ film was studied using X-ray photoelectron spectroscopy (XPS). In Fig. 3h, the core-level spectrum of Mo 3d exhibits two strong peaks at 228.9 and 232.0 eV corresponding to Mo⁴⁺ 3d_{5/2} and Mo⁴⁺ 3d_{3/2} (Mo-S bonding), respectively, and two weak peaks at 232.4 and 235.5 eV corresponding to Mo⁶⁺ 3d_{5/2} and Mo⁶⁺ 3d_{3/2} (Mo-O bonding), respectively^{39,40}. The Mo-O bonding is attributed to MoO₃, which is contained in the MoS₂ target. The atomic fraction of Mo⁶⁺ 3d contained in the grown bilayer MoS₂ is ~10.55%. Notably, no additional peak is observed at the low binding energy of ~229.0 eV, which corresponds to metallic 1T-MoS₂ or metal Mo⁴⁺. This indicates that the sputtered MoS₂ is fully sulfurized to form 2H-MoS₂ without a 1T-MoS₂ component. In addition, Fig. 3i shows two S 2p peaks at 161.8 and 163.0 eV, corresponding to the doublet

of S²⁻ 2p_{3/2} and S²⁻ 2p_{1/2}, respectively, which further confirms the 2H-MoS₂ crystal structure. The calculated atomic ratio between S²⁻ 2p and Mo⁴⁺ 3d is ~2.14, indicating a S-rich MoS₂ with good crystallinity grown via the two-step method.

Ultraviolet photoelectron spectroscopy analysis was used to study the electronic structure of the synthesized MoS₂ film under ultra-high vacuum using He I as a monochromatic excitation source. The work function (Φ) can be calculated using Φ = hv - W, where hv is the incident photon energy of 21.22 eV (He I) and W is the spectral width extracted from the intersection of the slope of the secondary cut-off spectrum with the baseline (Fig. 3j). The measured work function for the MoS₂ film is 4.40 eV, for which the value is consistent with the other reports⁴²⁻⁴⁵. In addition, the valence band maximum (VBM) can also be determined from the intersection of the slope of the first state from Fermi energy (E_F = 0 eV) with the baseline (Fig. 3k). The extracted difference of energy between the E_F and VBM is 1.65 eV. As previous reports, the few-layer MoS₂ exhibit a bandgap from 1.29 to 1.9 eV and it could be inferred that the synthesized MoS₂ film was an n-type semiconductor⁴⁶.

Electrical characteristics of MoS₂ devices in the array. I-V characteristics were measured for the 64 phototransistors and

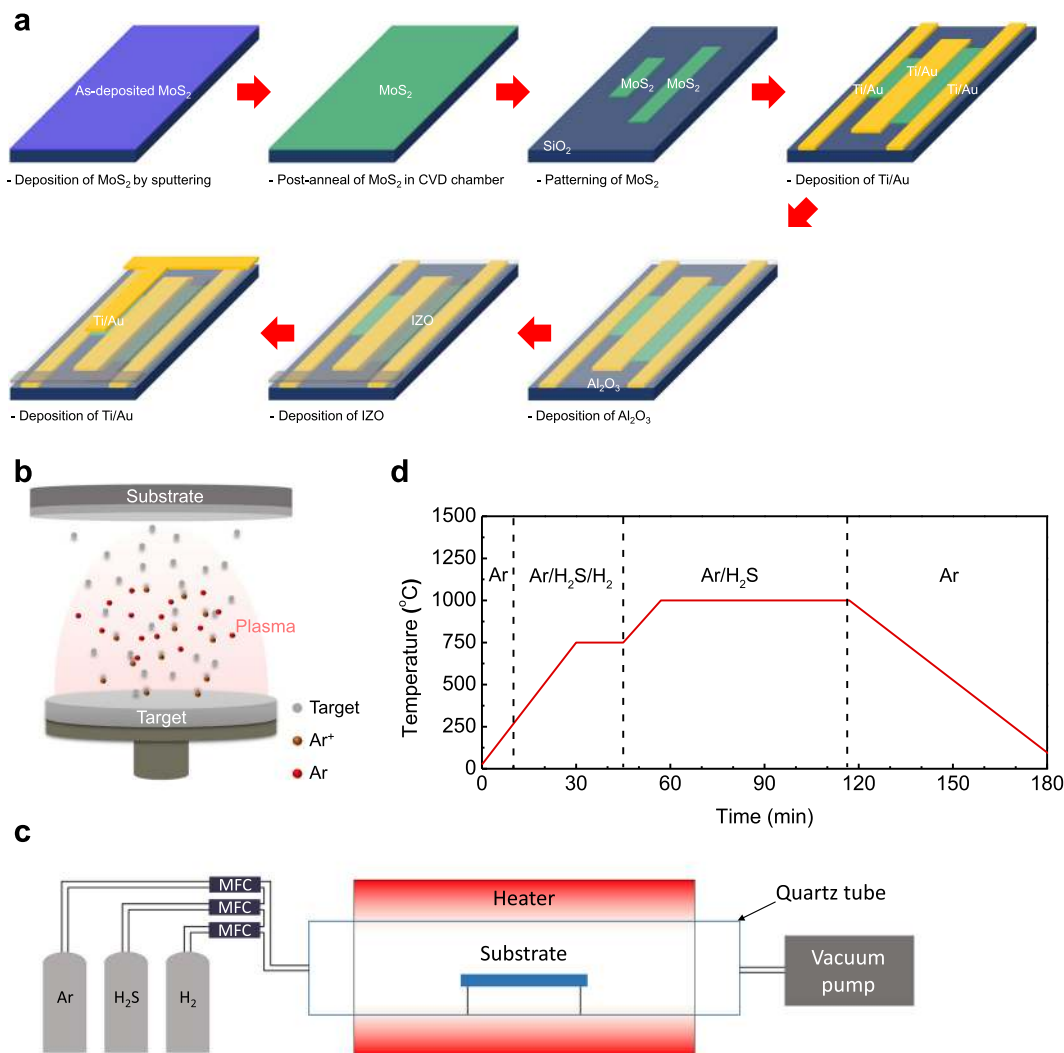


Fig. 2 Fabrication steps of the image sensor array based on bilayer MoS₂ film. **a** Fabrication process of a pixel unit cell in the proposed active pixel image sensor array with a bilayer MoS₂ film. Synthesis of a bilayer MoS₂ film using a two-step growth method: MoS₂ sputtering (first step) and sulfurization in the CVD (second step). Schematic image of **b** RF magnetron sputtering and **c** CVD chamber composed of gas sources (Ar, H₂S, H₂), quartz tube, heater, and vacuum pump. MFC is mass flow controller. **d** Temperature profile and gas injection conditions for sulfurization as a function of time. The vertical dashed lines divide four regions with different gas atmospheres.

64 switching transistors in the 8 × 8 active pixel image sensor array, to investigate its electrical properties. Figure 4a shows the transfer curves of a MoS₂ phototransistor in the active pixel image sensor array, indicating typical *n*-channel behaviors with a current on/off ratio ($I_{\text{on}}/I_{\text{off}}$) of 5.84×10^4 and a threshold voltage (V_{th}) of -22.32 V at a drain voltage (V_{ds}) of 5 V. Figure 4b also shows the output characteristics of the phototransistor. The drain current (I_{ds}) exhibits a linear behavior at a low drain bias due to the good ohmic contacts between the bilayer MoS₂ film and the S/D electrodes (Ti/Au), and shows a fully saturated current at a high drain bias due to the velocity-saturated charge carriers. Supplementary Fig. 3 shows comparison with the transfer curves of our bilayer, few-layer, and multilayer MoS₂ phototransistors under the back-gate and top-gate modulations. Bilayer MoS₂ exhibits the best performance than the other number of layers of MoS₂ grown by the two-step method. The electrical properties of MoS₂ phototransistors show metallic as the number of layer increase over the bilayer. Under back-gate modulation, the bilayer MoS₂ phototransistor shows improved electrical properties (red line) after Al₂O₃ passivation compared with that before Al₂O₃ passivation (black line). Under the top-gate modulation, the

electrical properties (blue line) of the device were significantly improved compared with that in the case of the back-gate modulation with the Al₂O₃ passivation layer (red line), which are attributed to the *n*-type doping effect^{47,48} and the high-*k* dielectric screening effect^{49,50} of the Al₂O₃ layer.

The statistical analysis of the electrical performance parameters of the 64 phototransistors in the active pixel image sensor array is summarized in Fig. 4c–e, which was obtained from the transfer curves of the 64 phototransistors as shown in Supplementary Fig. 4a. Figure 4c shows the distribution of the field-effect mobility (μ_{eff}), which is calculated from the following equation: $\mu_{\text{eff}} = g_m \frac{L_c}{W_c C_{\text{ox}} V_{\text{ds}}}$, where g_m is the transconductance, L_c and W_c are the length and width of the channel, respectively, C_{ox} is the capacitance of the gate insulator, and V_{ds} is the drain voltage. Furthermore, Fig. 4d, e show the distribution of the V_{th} and $I_{\text{on}}/I_{\text{off}}$. All the phototransistors exhibited a highly uniform performance with the following average values: a μ_{eff} of $4.85 \text{ cm}^2 \text{ V}^{-1} \text{ s}^{-1}$, a V_{th} of -23.65 V, and an $I_{\text{on}}/I_{\text{off}}$ of 3.88×10^4 . The 64 switching transistors were quantitatively analyzed using the above method repeatedly. Details of the switching transistors are shown in Supplementary Figs. 4b and 5.

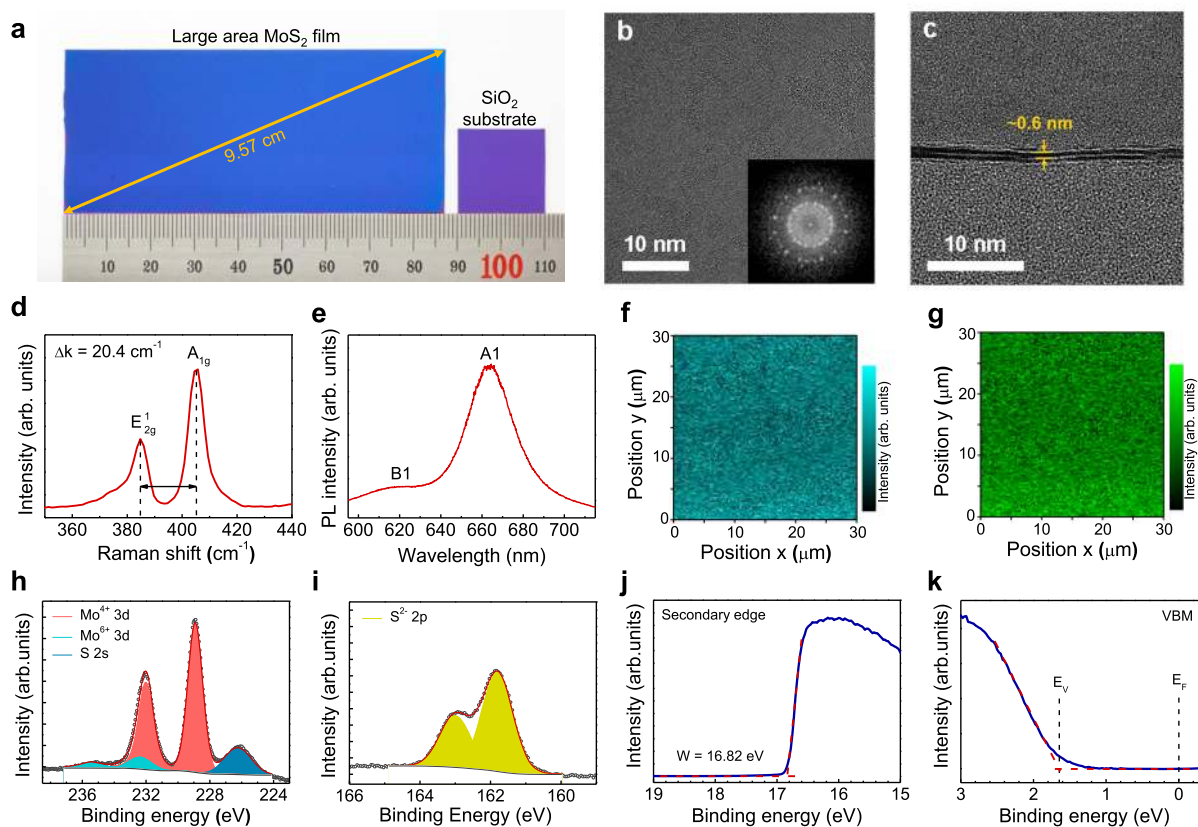


Fig. 3 Characterization of large-area bilayer MoS₂ film. **a** Photograph of a synthesized bilayer MoS₂ film on SiO₂/Si substrate (blue) comparison with a bare SiO₂/Si substrate (purple), indicating the color changes for before and after MoS₂ growth. **b** Plan-view and **c** cross-sectional TEM images of the bilayer MoS₂ film. The inset of **b** is a FFT pattern corresponding to the TEM image. **d** Raman and **e** PL spectrum of the bilayer MoS₂ film. **f**, **g** Raman mapping images of the intensity of E_{12g} and A_{1g} modes centered at 383 and 404 cm⁻¹, respectively. **h**, **i** XPS spectra of Mo 3d and S 2p core levels of the bilayer MoS₂ film, respectively. **j** Secondary cut-off and **k** valence band spectra obtained by UPS analysis of bilayer MoS₂ film.

Photoresponsive characteristics of MoS₂ devices in the array.

The proposed transparent top-gate phototransistor structure based on the bilayer MoS₂ active layer and IZO top-gate electrode in Fig. 1 can easily detect the incident light because of the light transmitted through the transparent top-gate electrode, even using an opaque SiO₂/Si substrate on which MoS₂ is directly grown without additional and complex processes (i.e., transferring MoS₂ onto glass or flexible substrate such as polyethylene terephthalate or polyimide films^{22,24,47}, resulting in low productivity and high cost). Figure 5a–c present the photoinduced transfer characteristics of the bilayer MoS₂ phototransistor in the active pixel image sensor array under red, green, and blue (RGB) light illumination with an excitation wavelength (λ_{ex}) of 638 nm (R), 532 nm (G), and 405 nm (B) at various incident power densities (P_{inc}) ranging from 0.1 to 3.2 mW cm⁻². The photocurrent of the bilayer MoS₂ phototransistor gradually increased with increasing P_{inc} . Figure 5d–f show the calculated photoresponsivity (R_{ph}), specific detectivity (D^*), and photosensitivity (S_{ph}) as functions of excitation wavelength and incident power density, which are important figures of merit for phototransistors. The R_{ph} was extracted from the transfer characteristics in Fig. 5a–c, using the equation of $R_{\text{ph}} = I_{\text{ph}}/P_{\text{inc}}$ (A W⁻¹), where I_{ph} and P_{inc} are the photocurrent and incident power density, respectively. The D^* was obtained by the equation of $D^* = \sqrt{A\Delta f}/\text{NEP} = R\sqrt{A\Delta f}/i_n$, where A is the channel area, Δf is the electrical bandwidth, NEP is the noise equivalent power, i_n is the noise current, and R is the responsivity at the same measurement conditions as the noise current (i_n)⁵¹. The noise

current, used to obtain the D^* , was measured by a lock-in amplifier (Supplementary Fig. 6). We obtained the S_{ph} defined as $S_{\text{ph}} = I_{\text{ph}}/I_{\text{dark}}$, where I_{dark} is the dark current, extracted from the transfer curves of the MoS₂ phototransistor. The maximum R_{ph} of 119.16 A W⁻¹ and D^* of 4.66×10^6 cm Hz^{1/2} W⁻¹ were obtained under the condition of $\lambda_{\text{ex}} = 405$ nm and $P_{\text{inc}} = 0.1$ mW cm⁻² for the former and $\lambda_{\text{ex}} = 532$ nm and $P_{\text{inc}} = 0.1$ mW cm⁻² for the latter. The maximum S_{ph} of 1173.44 was obtained at $\lambda_{\text{ex}} = 405$ nm and $P_{\text{inc}} = 3.2$ mW cm⁻². This is high R_{ph} reported for phototransistors with large-area synthesized MoS₂ films as shown in Supplementary Fig. 7 and Table 1.

The main mechanism for the high R_{ph} of the bilayer MoS₂ phototransistor is PG effect by the holes trapped at subgap states^{33,52–55}. The TEM and XPS analysis in Fig. 3 show that high density of grain boundaries, excess S, and a small amount of MoO₃ are present in the grown MoS₂ film. Previous works report that structural defects in MoS₂ itself can induce subgap states in the conduction and valence band^{56,57}. In Fig. 3k, a narrow distribution of states exists above the VBM in the bandgap. These band tail states near the valence band can capture the photogenerated holes, leading to the accumulation of positive charges and potential barrier lowering (i.e., PG effect). Injecting more electrons from the source by PG effect results in a significant enhancement of photoresponsivity in our MoS₂ phototransistor. Supplementary Fig. 8 shows the details of PG effect on the bilayer MoS₂ phototransistor through the extracted V_{th} shift (ΔV_{th}) and I_{ph} as a function of P_{inc} . Supplementary Fig. 8a exhibits $\Delta V_{\text{th}}-P_{\text{inc}}$ curves of the bilayer MoS₂

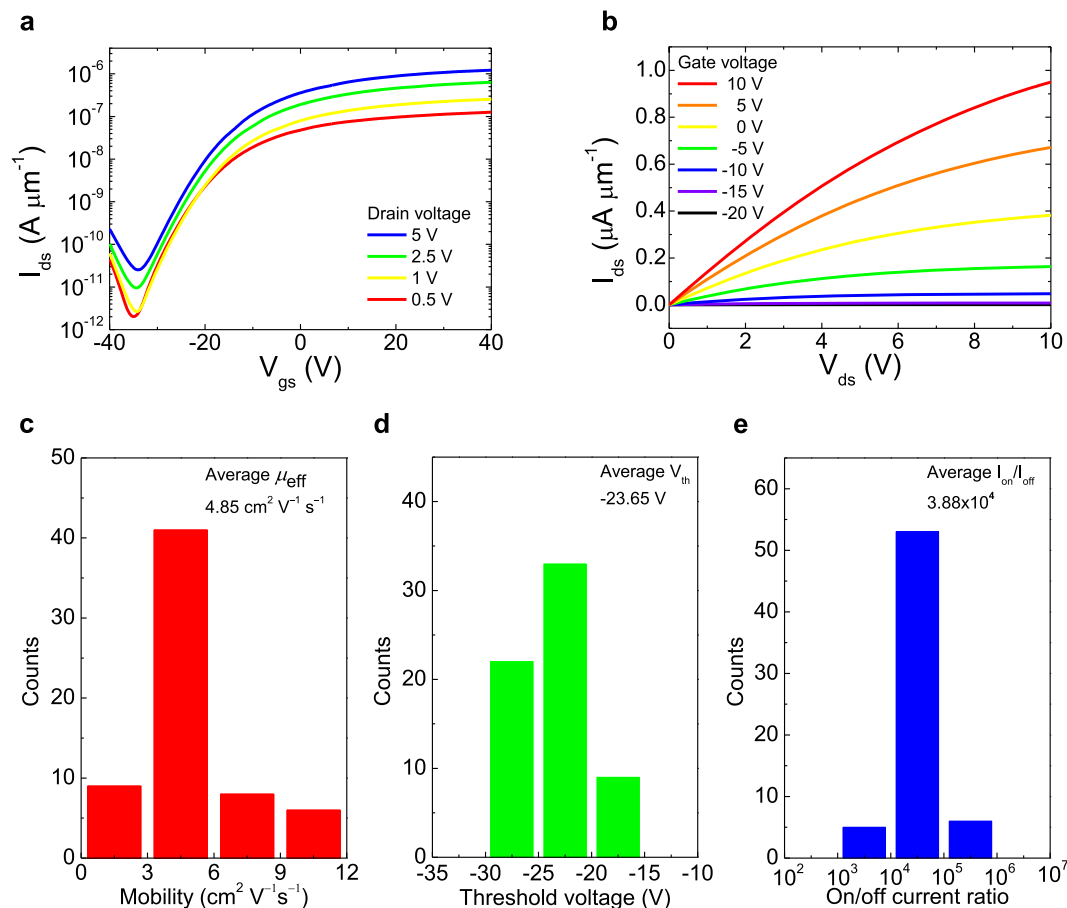


Fig. 4 Electrical characteristics and statistical analysis of phototransistors in bilayer MoS₂ image sensor array. **a** V_{gs} - I_{ds} curves of MoS₂ phototransistor at $V_{ds} = 0.5, 1, 2.5,$ and 5 V. **b** V_{ds} - I_{ds} curves of MoS₂ phototransistor at V_{gs} from -20 to 10 V with the gap of 5 V. Histograms of **c** field-effect mobility (average $\mu_{eff} = 4.85 \text{ cm}^2 \text{ V}^{-1} \text{ s}^{-1}$), **d** threshold voltage (average $V_{th} = -23.65$ V), and **e** on/off current ratio (average $I_{on}/I_{off} = 3.88 \times 10^4$) of the 64 MoS₂ phototransistors.

phototransistor under RGB light illumination. As depicted in the inset of Supplementary Fig. 8a, holes trapped at subgap states act as a local gate, resulting in the negative shift of V_{th} as the P_{inc} increased from 0.1 to 3.2 mW cm^{-2} . Supplementary Figs. 8b–d show the I_{ph} - P_{inc} curves of the device under RGB light illumination, respectively⁵³. By sweeping the gate voltage (V_{gs}) from -40 to 40 V, the slope of I_{ph} - P_{inc} (i.e., α : absorption coefficient) decreases, indicating that the dominant mechanism for R_{ph} high switches from photoconductive (PC) effect to PG effect^{33,54}. PC effect is that the conductivity of the channel is increased by the photogenerated electron–hole pairs, whereas PG effect is one of special PC effect resulted from accumulation of holes and conduction band lowering due to the defects, impurities, or multi-junction structure of channel materials. The PG effect affects similarly to the additional V_{gs} , resulting in decrease of α as the V_{gs} increases.

Figure 5g–i show the photoswitching behaviors of the bilayer MoS₂ phototransistor in the active pixel image sensor array under pulsed RGB light illumination with the frequency of 1 Hz. The rise time (τ_r) and fall time (τ_f) were defined as the times taken for the current to change from 20% to 80% and from 80% to 20% of the maximum current, respectively⁵⁸. The photoresponse speeds of the bilayer MoS₂ phototransistor under RGB light illumination were τ_r under R, τ_r under G, τ_r under B = $44, 85, 119$ ms and τ_f under R, τ_f under G, τ_f under B = $41, 52, 122$ ms, respectively. τ_r and τ_f increase as λ_{ex} decreases due to the greater number of photogenerated charge carriers. Such a satisfactory photoresponse speed indicates that the bilayer MoS₂ active pixel image sensor

array has the potential for fast image sensing. However, the response time still needs to be improved for high-speed imaging due to the trade-off relationship between response time and responsivity. Therefore, to improve the response speed of our image sensor array, we investigated the photoswitching characteristics of the bilayer MoS₂ phototransistor with gate pulse as shown in Supplementary Fig. 9. The 40 ms gate voltage pulse significantly enhanced the fall time from 104.8 ms to 22.99 ms due to the detrapping of the trapped holes at subgap states, enabling high-speed operation of the image sensor^{29,59–61}. Supplementary Table 2 shows the comparison of the photoresponse speed without and with gate pulse. The bilayer MoS₂ photodetector without a gate terminal in the same pixel was measured under the same conditions as in Fig. 5 to compare its photoresponsive characteristics with those of the proposed phototransistor (Supplementary Fig. 10). Consequently, compared with the photodetector without a gate terminal, the phototransistor showed significantly improved photoresponsivity, specific detectivity, and photosensitivity (i.e., SNR) by $14.01, 6.68,$ and 505.79 times, respectively.

Simulation results of bilayer MoS₂ phototransistor. To support the interpretation regarding the high R_{ph} of the bilayer MoS₂ phototransistor being induced by the PG effect, numerical device simulations were carried out. The simulation framework is based on the drift-diffusion formalism (see “Simulation methods” for details of the simulation setup) with material and device

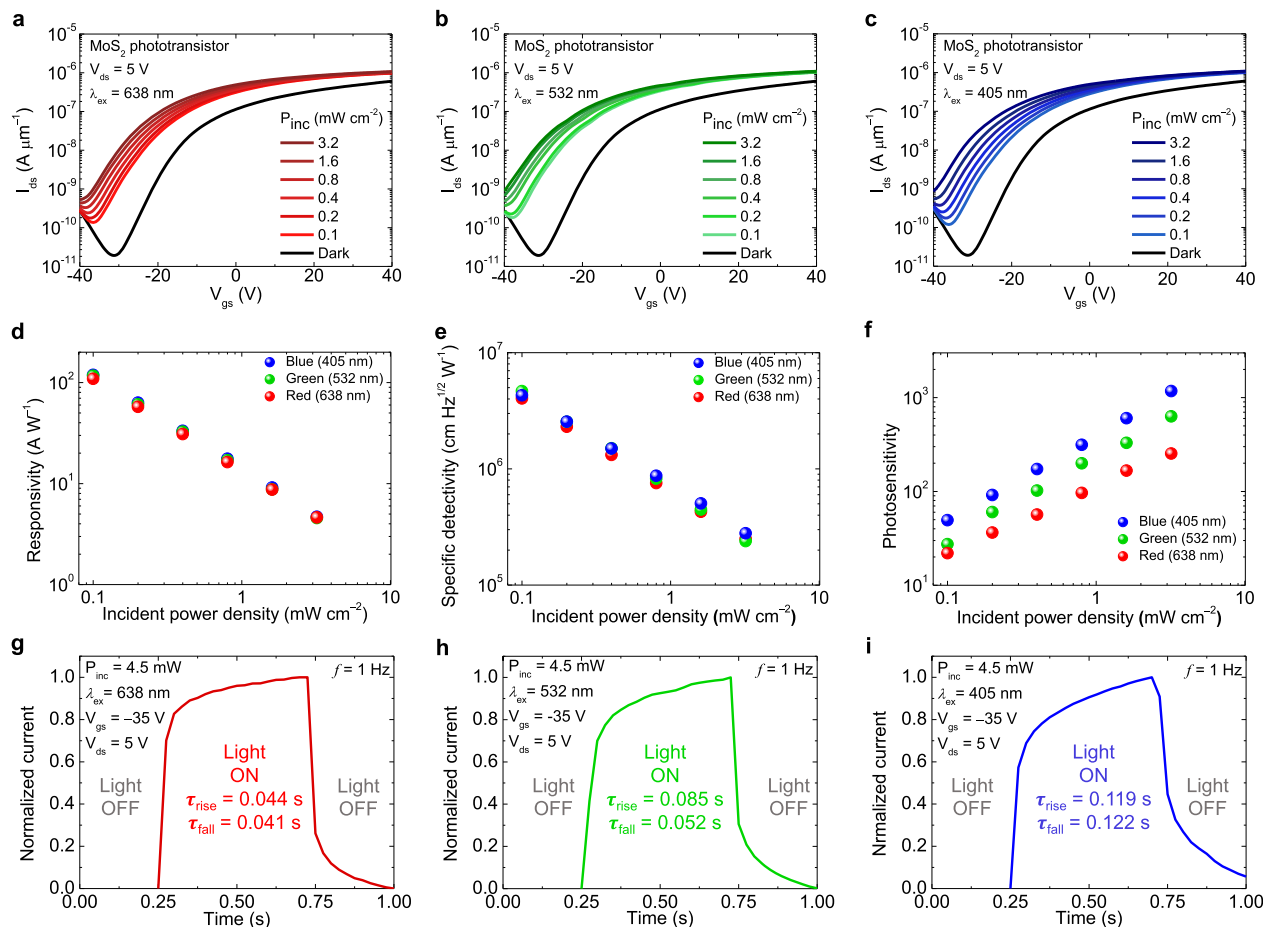


Fig. 5 Photoresponsive characteristics of a bilayer MoS₂ phototransistor in the image sensor array. I_{ds} - V_{gs} curves of a transparent top-gate phototransistor based on bilayer MoS₂ channel and IZO top-gate at $V_{ds} = 5$ V under **a** red, **b** green, and **c** blue light illumination with various incident power densities ($\lambda_{ex} = 638$ nm (R), 532 nm (G), and 405 nm (B), and $P_{inc} = 0.1, 0.2, 0.4, 0.8, 1.6, 3.2$ mW cm^{-2}). **d** Photoresponsivity, **e** specific detectivity, and **f** photosensitivity of the MoS₂ phototransistor under R, G, B light illumination calculated from Fig. 4a-c. **g-i** Photoswitching characteristics of the MoS₂ phototransistor under temporal light illumination with $\lambda_{ex} = 638, 532,$ and 405 nm, respectively. All switching curves were measured at $V_{ds} = 5$ V, $V_{gs} = -35$ V, and $P_{inc} = 4.5$ mW cm^{-2} with illumination frequency of 1 Hz. Rise and fall times were extracted from 20% to 80% and from 80% to 20% of the maximum current, respectively.

parameters set according to the experimental values derived from Fig. 3. The device structure implemented in the simulator is schematically represented in Fig. 6a (geometrical dimensions and electrical parameters adopted in the simulations are reported in the Supplementary Note 1). The simulated I_{ds} - V_{gs} and I_{ds} - V_{ds} curves in the dark (i.e., with no optically generated carriers) are shown in Fig. 6b, c, respectively. The V_{th} of the device under no illumination is ≈ -20 V and was calibrated by assuming that the Fermi energy (E_F) at equilibrium is close to the conduction band edge (E_C). This was simulated by including a large doping density ($N_D = 5 \times 10^{19} \text{ cm}^{-3}$) in the MoS₂ channel.

The simulated I_{ds} - V_{gs} curves under different light illumination conditions (each corresponding to a specific incident power density, P_{inc}) are shown in Fig. 6d. As it can be noticed, simulations correctly anticipate the large photoresponsivity observed experimentally (see Fig. 6e), which is attributed to the negative V_{th} shift as shown in Fig. 6f. This behavior was reproduced by including a defect level at 0.2 eV from the valence band edge (E_V), mimicking the narrow distribution of states above the VBM in the bandgap (see Fig. 3k). The trap state is of the donor-like type, i.e., positively charged (neutral) when filled (empty) of holes. As these traps are 0.2 eV above E_V , they tend to become easily filled with holes, the latter being provided by light. When traps capture the optically generated holes, they become

positively charged and thus cause V_{th} to decrease (Fig. 6f), in turn leading to the high R_{ph} (Fig. 6e) as also observed in the experiments (Fig. 5d). Interestingly, when performing simulations without including the trap states, the observed current modulation was relatively weak and inconsistent with experimental results. For example, Fig. 6d shows the simulated I_{ds} - V_{gs} without traps (gray lines, shifted to the right for better readability). In this case, no appreciable V_{th} shift is observed as shown in Fig. 6f. This leads to a much lower R_{ph} , as shown Fig. 6e. Figure 6g shows the trapped charge density (N_T^+) at $V_{gs} = -20$ V in the dark and with light illumination, clearly indicating that more holes are trapped in the latter case than in the former. Figure 6h,i show the simulated band diagrams corresponding to dark and with light illumination conditions with and without the inclusion of the trap states, respectively. The comparison of the two cases shows the high conductivity modulation occurring in the simulation with the inclusion of traps (Fig. 6h) and the weak variation occurring in the case without traps (Fig. 6i). All these results corroborate the hypothesis of PG effect being responsible for high R_{ph} .

Image sensing of bilayer MoS₂ image sensor array. The photoinduced transfer characteristics of all the 64 phototransistors were measured under a light illumination with a λ_{ex} of 638, 532,

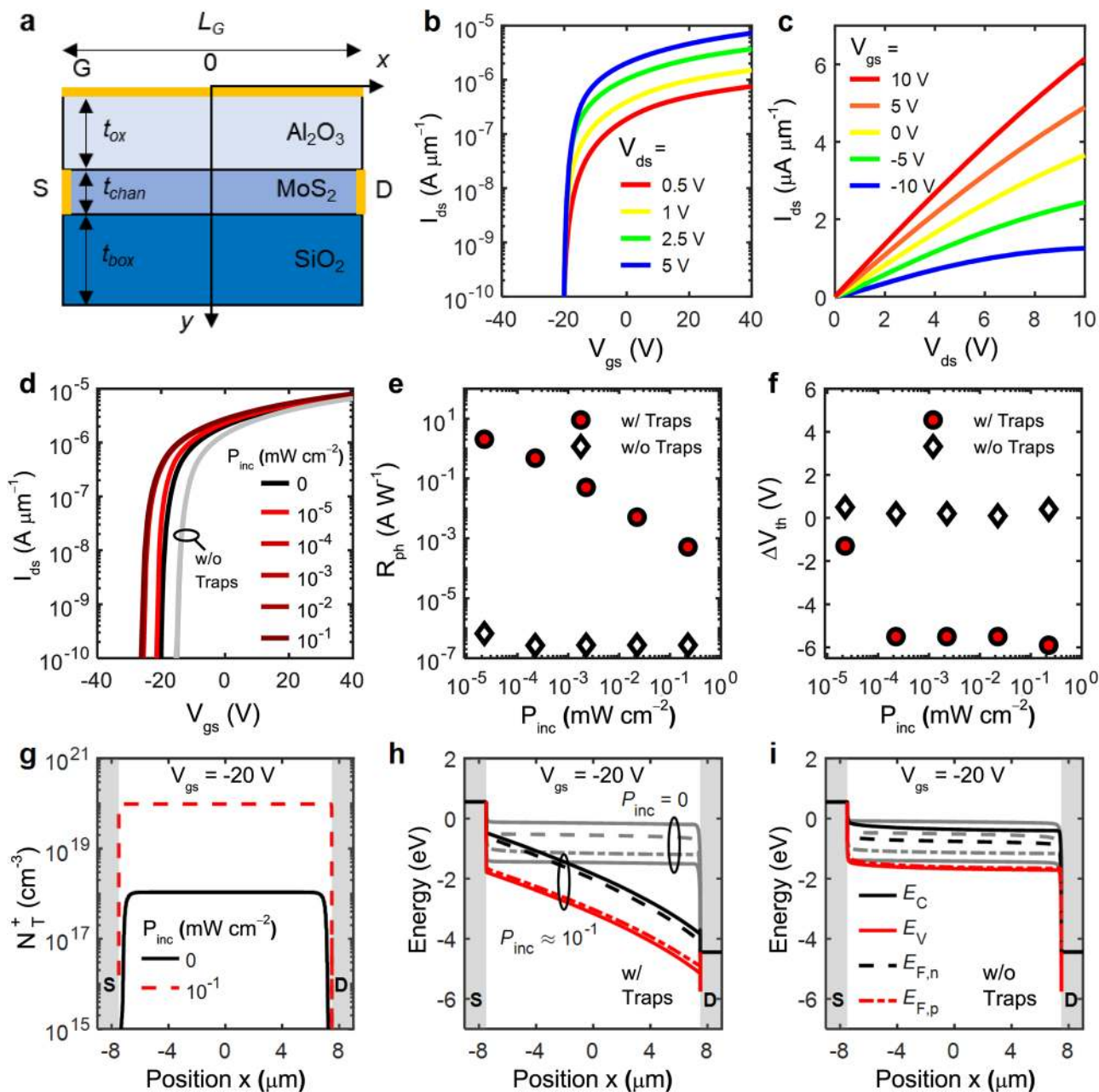


Fig. 6 Simulation results. **a** Sketch of the simulated 2D device. L_G , t_{ox} , t_{chan} , t_{box} , S, D, and G are gate length, gate oxide thickness, MoS₂ channel thickness, buried oxide thickness, source, drain, and gate, respectively. **b, c** Simulated I_{ds} - V_{gs} and I_{ds} - V_{ds} curves in the dark. **d** Simulated I_{ds} - V_{gs} under light illumination, for different incident power densities (P_{inc}). Simulated I_{ds} - V_{gs} curves without traps are also included for comparison (gray lines, shifted to the right for better visibility). **e, f** Photoresponsivity (R_{ph}) and Threshold Voltage Shift (ΔV_{th}) vs. P_{inc} extracted from the I_{ds} - V_{gs} simulation with and without traps, showing the correlation between high R_{ph} and negative ΔV_{th} . **g** Trapped charge density (N_T^+) at $V_{gs} = -20$ V in the dark ($P_{inc} = 0$ mW cm⁻², black line) and under light illumination ($P_{inc} \approx 10^{-1}$ mW cm⁻², red-dashed line). **h, i** Simulated energy band diagrams at $V_{gs} = -20$ V in the dark ($P_{inc} = 0$ mW cm⁻², gray lines) and under light illumination ($P_{inc} \approx 10^{-1}$ mW cm⁻², black and red lines) with (**h**) and without traps (**i**). X-axis in **g-i** is the position along the channel from source to drain contacts (indicated by the shaded gray bands).

and 405 nm at a fixed P_{inc} of 3.2 mW cm⁻², to investigate the photoresponse uniformity of the active pixel image sensor array. Figure 7a–c show the extracted photocurrent mapping of the 8 × 8 active pixel image sensor array achieved using the photoinduced transfer characteristics of the 64 phototransistors under RGB light illumination. Consequently, it is confirmed that the active pixel image sensor array has a high photoresponse uniformity for all the RGB light illumination conditions. The cross-talk characteristics between adjacent pixels were also investigated, resulting in negligible cross-talk between adjacent pixels (Supplementary

Fig. 11). Supplementary Fig. 12 shows the grayscale variation under various incident power densities. Moreover, a designed turtle stencil (total 24 × 24 pixels) was prepared and patterned using a laser cutting system as shown in Fig. 7d and Supplementary Video 1, to investigate the image-sensing characteristics of the 8 × 8 active pixel image sensor array. The stencil separated into nine pieces (Fig. 7e) is sequentially placed on the active pixel image sensor array during light projection (Fig. 7f). The measurement method using the light stencil projection is described in detail in Fig. 7g and the “Methods” section. Figure 7h shows the

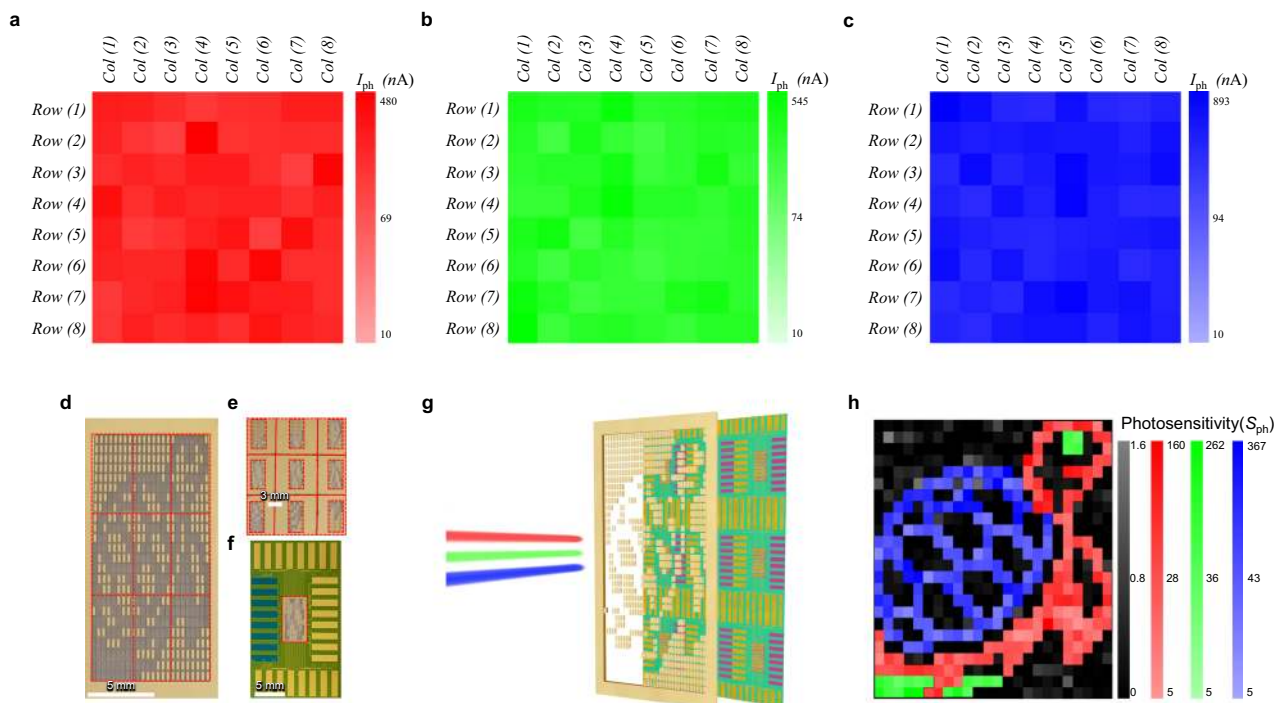


Fig. 7 Image-sensing characteristics of 8×8 bilayer MoS_2 image sensor array. **a–c** Photocurrent mapping of 64 MoS_2 phototransistors at $V_{ds} = 1\text{ V}$, $V_{gs} = -10\text{ V}$ under RGB light illumination ($\lambda_{ex} = 638, 532,$ and 405 nm and $P_{inc} = 3.2\text{ mW cm}^{-2}$), indicating uniform photocurrent photoresponses. **d** Photograph of the designed turtle stencil for projection (total 24×24 pixels). **e** Separated turtle stencils for individual light stencil projection on 8×8 image sensor array. **f** Top view of the image sensor array covered with a piece of separated turtle stencils. **g** Measurement concept using the light stencil projection for image detection of the image sensor array. The 8×8 bilayer MoS_2 image sensor array is placed behind turtle stencil and measured electrical properties under RGB light illumination ($\lambda_{ex} = 638, 532,$ and 405 nm). **h** Photosensitivity mapping result extracted from image detection of bilayer MoS_2 image sensor array.

photosensitivity mapping result of the active pixel image sensor array obtained through the light stencil projection, indicating successful turtle image sensing (the image pixel resolution is 576 pixels). This is due to the unique pixel structure in the active pixel image sensor array composed of opaque top-gate switching transistors and transparent top-gate phototransistors. As the top-gate electrode and block layer, the Au film covers the switching transistor in the pixels to remove the photocurrent interference of the switching transistor by light illumination during the image sensing through the active matrix as shown in Fig. 1. As mentioned earlier, the IZO top-gate electrode of the phototransistors enables light detection by the image sensor due to its transparent property.

Moreover, typical image signal process of complementary metal-oxide-semiconductor image sensor can be simply described as follows. First, the incident light is converted into current by the image sensor array and then read out by integrated circuit; then, current is converted to a digital signal by analog-to-digital converter. After that, the digital values are transferred into image signal processor for image processing such as image quality improvement. Finally, image data are acquired through the input/output interface^{62,63}.

Discussion

We demonstrated an active pixel image sensor array based on a bilayer MoS_2 film. A large-area bilayer MoS_2 film was directly synthesized on a SiO_2/Si substrate via a two-step growth method without any transfer process. In particular, the active pixel image sensor array architecture comprised opaque top-gate switching transistors and transparent top-gate phototransistors achieved higher photoresponsive characteristics than those of photodetector without gate terminal. The main mechanism for the high R_{ph} of

the bilayer MoS_2 phototransistor is PG effect by the holes trapped at subgap states. This was confirmed by detailed, experimentally guided, numerical simulations that highlighted how the large photoresponsivity increase is a consequence of photo-excited hole trapping at subgap states close to the valence band edge. The 64 individual pixels in the 8×8 active pixel image sensor array successfully functioned under RGB light illumination. The desired photoresponsive performance and unique architecture of the proposed active pixel image sensor array can facilitate its use in next-generation image detection applications, such as ultra-thin image sensors, transparent image sensors, artificial-intelligence photosensors, and selective light-detecting imagers.

Methods

Growth of MoS_2 via the two-step method. A bilayer MoS_2 film was synthesized using a two-step method, consisting of RF magnetron sputtering and thermal CVD. *P*-type doped Si substrates covered with 300 nm-thick SiO_2 were used as the substrates. Prior to the deposition of MoS_2 via sputtering, the SiO_2/Si substrates were ultrasonically cleaned for 10 min each in acetone, isopropyl alcohol, and deionized water. A 50.8 mm-diameter MoS_2 target (99.9%) was used in the magnetron sputtering system. The chamber was maintained below the base pressure of 3×10^{-6} Torr after loading the substrates and at the working pressure of 10 mTorr with an Ar flow of 75 s.c.c.m. The MoS_2 target was pre-sputtered for 10 min before the deposition, to remove the oxide layer on it and to make the plasma stable. The thin MoS_2 films were deposited on the SiO_2/Si substrates at room temperature with the RF power of 50 W for 14 s.

The as-deposited MoS_2 film on the SiO_2/Si substrate was sulfurized in a 2 inch CVD chamber. The chamber was pumped to a low vacuum, and then Ar was injected with a flow rate of 50 s.c.c.m. For the growth of MoS_2 , the temperature was ramped up to 750 °C in 30 min and maintained for 15 min. A gas mixture of H_2 (5 s.c.c.m.) and H_2S (5 s.c.c.m.) was injected into the chamber when the temperature reached 300 °C. Subsequently, an annealing process was performed at 1000 °C for 1 h under an Ar (50 s.c.c.m.) and H_2S (5 s.c.c.m.) atmosphere. The furnace was rapidly cooled to room temperature under an Ar flow at a rate of 50 s.c.c.m.

MoS₂ phototransistor fabrication. The MoS₂ film was deposited on the SiO₂/Si substrate for 14 s via RF magnetron sputtering, and then sulfurized at 750 °C and successively annealed at 1000 °C for 1 h in the CVD chamber, to fabricate the active pixel image sensor array with the bilayer MoS₂ film. Conventional photolithography was used to pattern the MoS₂ channel. A photoresist was spin-coated for 30 s at 3000 r.p.m. on the MoS₂ film. Afterward, the coated photoresist layer was exposed to UV light for 1 s and removed with a developer, which covered only the MoS₂ channel. The uncovered MoS₂ film was etched with O₂ plasma at the power of 10 W for 10 s. The photoresist remaining on the MoS₂ film was removed by spraying acetone. A lift-off resist and the photoresist were sequentially coated using a spin-coater for 45 s at 2000 r.p.m. and 30 s at 3000 r.p.m., respectively. Following that, they were removed via exposure to UV light. Afterward, the MoS₂ film was subjected to development processes to pattern electrodes. Subsequently, 10 nm titanium and 50 nm gold were deposited as electrodes via electron-beam evaporation and patterned via a lift-off process using photoresist remover. An 80 nm-thick Al₂O₃ as the top-gate insulator was then deposited on the lifted-off sample by ALD at 100 °C. Subsequently, IZO was deposited as the top-gate electrodes using a sputtering system. For the chemical etching of the IZO film after patterning, the sample was immersed in buffered oxide etching for 20 s. After patterning the transparent top-gate electrodes, Ti/Au (20/50 nm) were deposited by electron-beam evaporation and pattern by the lift-off process as the opaque top-gate electrodes. Finally, via holes were patterned using the aforementioned conventional photolithography and chemical etching processes sequentially.

Characterization of MoS₂. The surface of the MoS₂ film grown on the SiO₂/Si substrates was observed using optical microscopy (BX51M, Olympus, Co.) The heights of the bilayer MoS₂ films were measured using atomic force microscopy (XE7, PSIA Co.) in non-contact mode. Raman and PL spectra were obtained using a micro-Raman spectrometer system (ALPHA300, WITec, Co.) with an excitation laser at 532 nm at the MEMS-Sensor Platform Center of SungKyunKwan University (SKKU). XPS (Theta Probe AR-XPS System, ThermoFisher Scientific) measurements were performed with Al K α X-ray radiation (1486.6 eV). The working pressure in the ultra-high-vacuum chamber during the measurement was maintained below 3×10^{-9} mbar. C 1s at 284.5 eV was used for the calibration of the binding energies. The atomic image of MoS₂ was characterized using TEM (JEM ARM 200F, JEOL). The cross-sectional TEM imaging samples were fabricated using a focused ion beam system (NX2000, HITACHI). The electrical and photoresponse properties of the MoS₂ active pixel image sensor array were characterized using a semiconductor characterization system (4200 SCS, Keithley) and multi-channel fiber-coupled laser source (MCLS1, Thorlabs) in an ambient condition. The noise current of the MoS₂ phototransistor was measured using a lock-in amplifier (SR830 lock-in amplifier, Stanford Research Systems). The image-sensing characteristics of the active pixel image sensor array were measured using light stencil projection. The turtle stencil (24 \times 24 pixels) was patterned onto the gold-deposited glass using a laser cutting system. The turtle stencil separated into nine pieces (8 \times 8 pixels) was sequentially placed on the 8 \times 8 active pixel image sensor array. Subsequently, the individual pixels were measured by connecting the contact pads adjacent to the edge of the substrate under a light projection. To obtain the colored image, each pixel of the image sensor array was measured with the turtle stencil under RGB light that differs from pixel to pixel, respectively. The light stencil projection method was inspired and developed from previous reports^{30,64}. Lee et al.³⁰ reported a single-pixel imager and the image scanning system with three different light sources (RGB).

Simulation methods. The 2D numerical simulations model the carrier transport problem with the drift-diffusion formalism (see Supplementary Note 1 for the full equation set). This way, Poisson equation and continuity equations are solved self-consistently for each applied bias (in terms of gate-to-source and drain-to-source voltage), to obtain the electrostatic potential and the carriers' concentration. For simplicity, the light source is considered ideal, i.e., it provides constant electron-hole pair generation rates. Shockley-Read-Hall formalism was adopted to model trap capture and emission dynamics.

Data availability

The data that support the findings of this study are available from the corresponding author upon reasonable request.

Received: 25 February 2021; Accepted: 10 May 2021;

Published online: 11 June 2021

References

- Xia, F., Wang, H., Xiao, D., Dubey, M. & Ramasubramaniam, A. Two-dimensional material nanophotonics. *Nat. Photonics* **8**, 899–907 (2014).
- Nourbakhsh, A., Zubair, A., Joglekar, S., Dresselhaus, M. & Palacios, T. Subthreshold swing improvement in MoS₂ transistors by the negative capacitance effect in a ferroelectric Al-doped-HfO₂/HfO₂ gate dielectric stack. *Nanoscale* **9**, 6122–6127 (2017).
- Rhyee, J.-S. et al. High-mobility transistors based on large-area and highly crystalline CVD-grown MoSe₂ films on insulating substrates. *Adv. Mater.* **28**, 2316–2321 (2016).
- Wang, Q. H., Kalantar-Zadeh, K., Kis, A., Coleman, J. N. & Strano, M. S. Electronics and optoelectronics of two-dimensional transition metal dichalcogenides. *Nat. Nanotechnol.* **7**, 699–712 (2012).
- Kaasbjerg, K., Thygesen, K. S. & Jacobsen, K. W. Phonon-limited mobility in n-type single-layer MoS₂ from first principles. *Phys. Rev. B* **85**, 115317 (2012).
- Roy, T. et al. Field-effect transistors built from all two-dimensional material components. *ACS Nano* **8**, 6259–6264 (2014).
- Kim, S. et al. High-mobility and low-power thin-film transistors based on multilayer MoS₂ crystals. *Nat. Commun.* **3**, 1–7 (2012).
- Yin, Z. et al. Single-layer MoS₂ phototransistors. *ACS Nano* **6**, 74–80 (2012).
- Choi, W. et al. High-detectivity multilayer MoS₂ phototransistors with spectral response from ultraviolet to infrared. *Adv. Mater.* **24**, 5832–5836 (2012).
- Li, D. et al. Two-dimensional non-volatile programmable p–n junctions. *Nat. Nanotechnol.* **12**, 901–906 (2017).
- Ling, X. et al. Parallel stitching of 2D materials. *Adv. Mater.* **28**, 2322–2329 (2016).
- Cheng, R. et al. High-performance, multifunctional devices based on asymmetric van der Waals heterostructures. *Nat. Electron.* **1**, 356–361 (2018).
- Resta, G. V. et al. Doping-free complementary logic gates enabled by two-dimensional polarity-controllable transistors. *ACS Nano* **12**, 7039–7047 (2018).
- Wang, M. et al. Robust memristors based on layered two-dimensional materials. *Nat. Electron.* **1**, 130–136 (2018).
- Cheng, R. et al. Few-layer molybdenum disulfide transistors and circuits for high-speed flexible electronics. *Nat. Commun.* **5**, 1–9 (2014).
- Wang, H. et al. Integrated circuits based on bilayer MoS₂ transistors. *Nano Lett.* **12**, 4674–4680 (2012).
- Naqi, M. et al. Ultrasensitive multilayer MoS₂-based photodetector with permanently grounded gate effect. *Adv. Electron. Mater.* **6**, 1901256 (2020).
- Wang, L. et al. Electronic devices and circuits based on wafer-scale polycrystalline monolayer MoS₂ by chemical vapor deposition. *Adv. Electron. Mater.* **5**, 1900393 (2019).
- Polyushkin, D. K. et al. Analogue two-dimensional semiconductor electronics. *Nat. Electron.* **3**, 486–491 (2020).
- Woo, Y. et al. Large-area CVD-grown MoS₂ driver circuit array for flexible organic light-emitting diode display. *Adv. Electron. Mater.* **4**, 1800251 (2018).
- Jayachandran, D. et al. A low-power biomimetic collision detector based on an in-memory molybdenum disulfide photodetector. *Nat. Electron.* **3**, 646–655 (2020).
- Choi, M. et al. Full-color active-matrix organic light-emitting diode display on human skin based on a large-area MoS₂ backplane. *Sci. Adv.* **6**, eabb5898 (2020).
- Zhang, T. et al. Fast-response inverter arrays built on wafer-scale MoS₂ by atomic layer deposition. *Phys. Stat. Solid. RRL* **13**, 1900018 (2019).
- Choi, C. et al. Human eye-inspired soft optoelectronic device using high-density MoS₂-graphene curved image sensor array. *Nat. Commun.* **8**, 1–11 (2017).
- Jang, H. et al. An atomically thin optoelectronic machine vision processor. *Adv. Mater.* **32**, 2002431 (2020).
- Lee, W. et al. High-resolution spin-on-patterning of perovskite thin films for a multiplexed image sensor array. *Adv. Mater.* **29**, 1702902 (2017).
- Goossens, S. et al. Broadband image sensor array based on graphene-CMOS integration. *Nat. Photonics* **11**, 366–371 (2017).
- Wong, W. S., Raychaudhuri, S., Lujan, R., Sambandan, S. & Street, R. A. Hybrid Si nanowire/amorphous silicon FETs for large-area image sensor arrays. *Nano Lett.* **11**, 2214–2218 (2011).
- Lopez-Sanchez, O., Lembke, D., Kayci, M., Radenovic, A. & Kis, A. Ultrasensitive photodetectors based on monolayer MoS₂. *Nat. Nanotechnol.* **8**, 497–501 (2013).
- Lee, Y. T. et al. High-performance 2D MoS₂ phototransistor for photo logic gate and image sensor. *ACS Photonics* **5**, 4745–4750 (2018).
- Kim, T.-Y. et al. Transparent large-area MoS₂ phototransistors with inkjet-printed components on flexible platforms. *ACS Nano* **11**, 10273–10280 (2017).
- Hong, S. et al. Sensory adaptation and neuromorphic phototransistors based on CsPb(Br_{1-x}I_x)₃ perovskite and MoS₂ hybrid structure. *ACS Nano* **14**, 9796–9806 (2020).
- Park, H. et al. Exceptionally uniform and scalable multilayer MoS₂ phototransistor array based on large-scale MoS₂ grown by RF sputtering, electron beam irradiation, and sulfurization. *ACS Appl. Mater. Interfaces* **12**, 20645–20652 (2020).
- Xu, J., Zhang, J., Zhang, W. & Lee, C.-S. Interlayer nanoarchitectonics of two-dimensional transition-metal dichalcogenides nanosheets for energy storage and conversion applications. *Adv. Energy Mater.* **7**, 1700571 (2017).

35. Li, H. et al. From bulk to monolayer MoS₂: evolution of Raman scattering. *Adv. Funct. Mater.* **22**, 1385–1390 (2012).
36. Lee, C. et al. Anomalous lattice vibrations of single- and few-layer MoS₂. *ACS Nano* **4**, 2695–2700 (2010).
37. Chu, T., Ilatikhameneh, H., Klimeck, G., Rahman, R. & Chen, Z. Electrically tunable bandgaps in bilayer MoS₂. *Nano Lett.* **15**, 8000–8007 (2015).
38. Splendiani, A. et al. Emerging photoluminescence in monolayer MoS₂. *Nano Lett.* **10**, 1271–1275 (2010).
39. Brown, N. M., Cui, N. & McKinley, A. An XPS study of the surface modification of natural MoS₂ following treatment in an RF-oxygen plasma. *Appl. Surf. Sci.* **134**, 11–21 (1998).
40. Liu, N. et al. Large-area atomically thin MoS₂ nanosheets prepared using electrochemical exfoliation. *ACS Nano* **8**, 6902–6910 (2014).
41. Hussain, S. et al. Large-area, continuous and high electrical performances of bilayer to few layers MoS₂ fabricated by RF sputtering via post-deposition annealing method. *Sci. Rep.* **6**, 1–13 (2016).
42. Huang, F. et al. The influence of interfacial tensile strain on the charge transport characteristics of MoS₂-based vertical heterojunction devices. *Nanoscale* **8**, 17598–17607 (2016).
43. Yun, J.-M. et al. Efficient work-function engineering of solution-processed MoS₂ thin-films for novel hole and electron transport layers leading to high-performance polymer solar cells. *J. Mater. Chem. C* **1**, 3777–3783 (2013).
44. Jiao, K. et al. The role of MoS₂ as an interfacial layer in graphene/silicon solar cells. *Phys. Chem. Chem. Phys.* **17**, 8182–8186 (2015).
45. Tarasov, A. et al. Controlled doping of large-area trilayer MoS₂ with molecular reductants and oxidants. *Adv. Mater.* **27**, 1175–1181 (2015).
46. Ganatra, R. & Zhang, Q. Few-layer MoS₂: a promising layered semiconductor. *ACS Nano* **8**, 4074–4099 (2014).
47. Choi, M. et al. Flexible active-matrix organic light-emitting diode display enabled by MoS₂ thin-film transistor. *Sci. Adv.* **4**, eaas8721 (2018).
48. Hong, S. et al. n-Type doping effect of CVD-grown multilayer MoSe₂ thin film transistors by two-step functionalization. *Adv. Electron. Mater.* **4**, 1800308 (2018).
49. Li, T., Wan, B., Du, G., Zhang, B. & Zeng, Z. Electrical performance of multilayer MoS₂ transistors on high-κ Al₂O₃ coated Si substrates. *AIP Adv.* **5**, 057102 (2015).
50. Bolshakov, P. et al. Improvement in top-gate MoS₂ transistor performance due to high quality backside Al₂O₃ layer. *Appl. Phys. Lett.* **111**, 032110 (2017).
51. Konstantatos, G. et al. Ultrasensitive solution-cast quantum dot photodetectors. *Nature* **442**, 180–183 (2006).
52. Kim, S. et al. Interstitial Mo-assisted photovoltaic effect in multilayer MoSe₂ phototransistors. *Adv. Mater.* **30**, 1705542 (2018).
53. Buscema, M. et al. Photocurrent generation with two-dimensional van der Waals semiconductors. *Chem. Soc. Rev.* **44**, 3691–3718 (2015).
54. Fang, H. & Hu, W. Photogating in low dimensional photodetectors. *Adv. Sci.* **4**, 1700323 (2017).
55. Butt, N. Z., Sarker, B. K., Chen, Y. P. & Alam, M. A. Substrate-induced photofield effect in graphene phototransistors. *IEEE Trans. Electron Devices* **62**, 3734–3741 (2015).
56. Furchi, M. M., Polyushkin, D. K., Pospischil, A. & Mueller, T. Mechanisms of photoconductivity in atomically thin MoS₂. *Nano Lett.* **14**, 6165–6170 (2014).
57. Zhu, W. et al. Electronic transport and device prospects of monolayer molybdenum disulphide grown by chemical vapour deposition. *Nat. Commun.* **5**, 1–8 (2014).
58. Früngel, F. B. *Optical Pulses-Lasers-Measuring Techniques* (Academic, 2014).
59. Jeon, S. et al. Gated three-terminal device architecture to eliminate persistent photoconductivity in oxide semiconductor photosensor arrays. *Nat. Mater.* **11**, 301–305 (2012).
60. Ahn, S. E. et al. Metal oxide thin film phototransistor for remote touch interactive displays. *Adv. Mater.* **24**, 2631–2636 (2012).
61. Sun, M. et al. Gate stimulated high-performance MoS₂-In(OH)_xSe phototransistor. *Nanotechnology* **31**, 095203 (2019).
62. Gove, R. J. *High Performance Silicon Imaging* (Elsevier, 2020).
63. Zhu, H. et al. in *2018 IEEE Asia Pacific Conference on Circuits and Systems (APCCAS)* 528–531 (IEEE).
64. Choi, H. T. et al. Zero-dimensional PbS quantum dot-InGaZnO film heterostructure for short-wave infrared flat-panel imager. *ACS Photonics* **7**, 1932–1941 (2020).

Acknowledgements

This research was supported in part by the National Research Foundation of Korea (2021R1A2B5B02002167, 2021M3H4A1A02056037, 2020H1D3A2A02103378, and 2020R1I1A1A01070907).

Author contributions

S.K. designed and supervised this project. S.H. performed all the experiments, except for the synthesis of MoS₂. S.C. performed the synthesis of MoS₂ and contributed to the experiments and spectroscopic analysis. S.B. and A.B. contributed to the synthesis of MoS₂. N.L. and H.Y. performed the spectroscopic analysis of MoS₂. B.H.K. and H.J.K. performed the IZO deposition. H.J.Y. performed the UPS measurement. N.Z. and M.A.A. conceived and performed the device modeling and numerical simulations. All the authors analyzed the data. S.H., N.Z., S.C., N.L., and S.K. wrote the manuscript. All the authors have approved the final version of the manuscript.

Competing interests

The authors declare no competing interests.

Additional information


Supplementary information The online version contains supplementary material available at <https://doi.org/10.1038/s41467-021-23711-x>.

Correspondence and requests for materials should be addressed to M.A.A. or S.K.

Peer review information *Nature Communications* thanks Xiaomu Wang, Do Kyung Hwang, and the other anonymous reviewers for their contribution to the peer review of this work.

Reprints and permission information is available at <http://www.nature.com/reprints>

Publisher's note Springer Nature remains neutral with regard to jurisdictional claims in published maps and institutional affiliations.

 **Open Access** This article is licensed under a Creative Commons Attribution 4.0 International License, which permits use, sharing, adaptation, distribution and reproduction in any medium or format, as long as you give appropriate credit to the original author(s) and the source, provide a link to the Creative Commons license, and indicate if changes were made. The images or other third party material in this article are included in the article's Creative Commons license, unless indicated otherwise in a credit line to the material. If material is not included in the article's Creative Commons license and your intended use is not permitted by statutory regulation or exceeds the permitted use, you will need to obtain permission directly from the copyright holder. To view a copy of this license, visit <http://creativecommons.org/licenses/by/4.0/>.

© The Author(s) 2021